Development of Lead Iodide Perovskite Solar Cells Using Three-Dimensional Titanium Dioxide Nanowire Architectures

Yanhao Yu,[†] Jianye Li,[†] Dalong Geng,[†] Jialiang Wang,[†] Lushuai Zhang,[†,‡] Trisha L. Andrew,[‡] Michael S. Arnold,[†] and Xudong Wang*[,†]

[†]Department of Materials Science and Engineering and [‡]Department of Chemistry, University of Wisconsin—Madison, Madison, Wisconsin 53706, United States

ABSTRACT Three-dimensional (3D) nanowire (NW) architectures are considered as superior electrode design for photovoltaic devices compared to NWs or nanoparticle systems in terms of improved large surface area and charge transport properties. In this paper, we report development of lead iodide perovskite solar cells based on a novel 3D TiO_2 NW architectures. The 3D TiO_2 nanostructure was synthesized via surface-reaction-limited pulsed chemical vapor deposition (SPCVD) technique that also implemented the Kirkendall effect for complete ZnO NW template conversion. It was found that the film thickness of 3D TiO_2 can significantly influence the photovoltaic performance. Short-circuit current increased with the TiO_2 length, while open-circuit voltage and fill factor decreased with the length. The highest power conversion efficiency (PCE) of 9.0% was achieved with ~600 nm long 3D TiO_2 NW structures. Compared to other 1D nanostructure arrays (TiO_2 nanotubes, TiO_2-coated ZnO NWs and ZnO NWs), 3D TiO_2 NW architecture was able to achieve larger amounts of perovskite loading, enhanced light harvesting efficiency, and increased electron-transport property. Therefore, its PCE is 1.5, 2.3, and 2.8 times higher than those of TiO_2 nanotubes, TiO_2-coated ZnO NWs, and ZnO NWs, respectively. The unique morphological advantages, together with the largely suppressed hysteresis effect, make 3D hierarchical TiO_2 a promising electrode selection in designing high-performance perovskite solar cells.

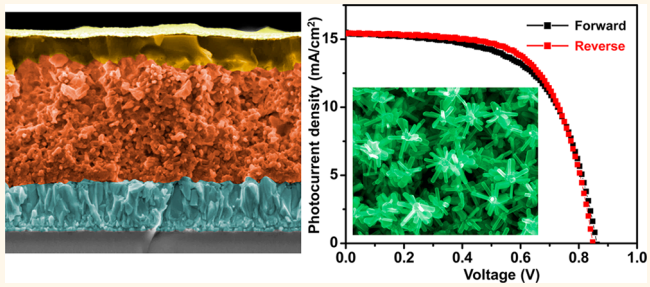

KEYWORDS: three-dimensional nanowires · titanium dioxide · $CH_3NH_3PbI_3$ · perovskite · solar cells

Rapid charge transport and high surface area are preferable characteristics for solar energy harvesting including photoelectrochemical (PEC) cells and dye-sensitized solar cells (DSSCs).[1] Single crystalline nanowires (NWs) and mesoporous nanoparticles (NPs) are representative structures with the merits of fast electron conducting and large surface area, respectively, whereas intrinsic limitations such as low surface area of NWs and poor electron mobility of NPs pronouncedly compensate their aforementioned advantages. Recently, three-dimensional (3D) hierarchical nanostructures have emerged as promising building blocks for photoelectrode design because they offer high-speed pathways as well as considerable surface area for sufficient chemical reaction or dye loading simultaneously.[2−4] Heterogeneous structures including Si/TiO_2,[5−7] Si/ZnO,[8−10] and CuO/ZnO[11] have demonstrated remarkable enhancement of efficiency in PEC water splitting compared to bare NW electrodes. Concurrently, homogeneous TiO_2-phase 3D nanostructures were found to be effective in DSSCs development and exhibited a fast electron-transport rate over randomly oriented NPs.[12−19] Substantial research efforts have notably boosted the power conversion efficiency (PCE) through fabrication of delicate hierarchical TiO_2 nanostructures. However, the low absorption coefficient of traditional organic dye limits further enhancement of 3D TiO_2-based DSSCs.[20,21]

Methylammonium lead iodide ($CH_3NH_3PbI_3$) is rising as a new star in the photovoltaic (PV) field because of its favorable direct band gap (1.55 eV) for good light absorption (entire visible light absorption), small

* Address correspondence to xudong@engr.wisc.edu.

Received for review October 14, 2014 and accepted December 30, 2014.

Published online December 30, 2014
10.1021/nn5058672

binding energy (about 0.030 eV) of excitons, high carrier mobility (7.5 $cm^2\ V^{-1}\ s^{-1}$ for electrons and 12.5 $cm^2\ V^{-1}\ s^{-1}$ for holes), and long charge diffusion length (ranging from 100 to 1000 nm).[22−29] PCEs of around 15% have been frequently reported on the basis of both planar and mesoscopic cell configurations.[30−37] Advantages of incorporating mesoporous NPs include facilitating charge collection and alleviating the hysteresis effect,[28,38,39] which is a severe issue that could over- or underestimate PCEs.[28,40−42] Besides mesoporous NPs, NWs have also been intensively investigated as the framework for supporting perovskite.[20,21,43,44] However, to date, there is still no practical study of 3D NW-based perovskite solar cells (SCs) although tremendous merits are intuitively expected. For instance, the large absorption coefficient of perovskite is highly desired for 3D NW-based SCs. The stem of the 3D structure could serve as a rapid charge-conducting channel to facilitate electron collection and possibly reduce the hysteresis effect in analogy with NPs. Compared to regular NW arrays, the 3D branched NW structure is able to provide a much higher volume density of nucleation sites for the deposition of perovskite and thus allows larger photoactive materials loading. Additionally, the entire treelike morphology could increase the optical pathways by light scattering.

In this paper, we report a 3D TiO_2 NW-based lead iodide perovskite SCs. A surface-reaction-limited pulsed chemical vapor deposition (SPCVD) technique was employed to fabricate the 3D TiO_2 architecture,[45] where the $CH_3NH_3PbI_3$ perovskite was deposited using the sequential deposition method.[30] The highest PCE yielded by the 3D TiO_2 structure was found to be 9.0%, which was substantially higher than perovskite SCs made from ZnO NWs, TiO_2-coated ZnO NWs, and TiO_2 nanotubes (NT). Over 8% of PCEs have been achieved on the basis of 3D TiO_2 with length variations ranging from ∼600 nm to ∼1.4 μm. Furthermore, enhanced light absorption at the visible light region, increased electron mobility, and low hysteresis effects were observed from the 3D TiO_2-based perovskite SCs.

RESULTS AND DISCUSSION

3D TiO_2 NW architecture was synthesized inside a homemade atomic layer deposition (ALD) system using ZnO NW arrays as the template and $TiCl_4$ and H_2O as the precursors. TiO_2 NT was formed after 10 cycles of deposition through the cation-exchange reaction governed by the Kirkendall effect.[45] Subsequently, the SPCVD process dominated the growth, forming high-density single crystalline TiO_2 nanorods (NRs) on the entire TiO_2 NT stem (see the Methods section for details). Figure 1a shows scanning electron microscopy (SEM) images of as-received treelike 3D TiO_2 NW structures (inset of Figure 1a). The interspace between individual TiO_2 nanostructures was from 160 to 430 nm, which was within the range of the grain size distribution of perovskite acquired from the sequential deposition approach, implying possible full $CH_3NH_3PbI_3$ coverage of the open space. TEM characterizations on a branched NW demonstrate the dense and uniform TiO_2 NR distribution along the entire trunk with a density of ∼70 NRs per μm (Figure 1b). The trunk is polycrystalline with a hollow center (Figure 1c), which manifests the Kirkendall effect induced by different ionic diffusion rates of the ZnO core and TiO_2 shell during the vapor-phase deposition.[45] The shell thickness of the TiO_2 NT core was found to be ∼12 nm. A high-resolution TEM (HRTEM) image reveals the high-quality lattice of single crystalline TiO_2 NRs which do not show any line or planar defects. Lattice spacing measured from the HRTEM image was 0.48 and 0.35 nm, perfectly matching the (002) and (011) planes of anatase TiO_2, respectively.[46,47] Besides the dominated anatase phase, rutile TiO_2 was also observed from the X-ray diffraction (XRD) pattern (Figure 1d), which was likely formed in the stem portion where foreign elements, such as Zn, were involved.[45]

Figure 2 shows cross-sectional SEM images of 3D TiO_2 NW architecture (Figure 2a), $CH_3NH_3PbI_3$ perovskite-coated TiO_2 (Figure 2b), and the complete PV devices (Figure 2c). The film thicknesses of perovskite were governed by the length of 3D TiO_2 NWs. Four different lengths were selected (∼600 nm, ∼1.0 μm, ∼1.4 μm, and ∼1.7 μm) and marked as i, ii, iii, and iv, respectively. The length of TiO_2 was controlled by the length of ZnO NW templates through adjustment of the synthesis period.[48] After sequential deposition of PbI_2 and CH_3NH_3I, $CH_3NH_3PbI_3$ perovskite could densely cover the entire 3D TiO_2 NW architecture with a film thickness up to ∼1.4 μm (Figure 2b, i−iii), indicating a large loading amount of photoactive perovskite. Such an efficient perovskite loading benefited from the high density TiO_2 branch that serves as the nucleation site for perovskite formation. For the shortest TiO_2 scaffolds, large-sized perovskite crystals with sizes of 120 to 450 nm were also formed and nearly covered the entire top area. Longer TiO_2 structures possess larger space in between, and fewer perovskite crystals were observed on the top (Figure S1, Supporting Information). When the TiO_2 thickness increased to ∼1.7 μm, an uncovered region around the top of TiO_2 could be observed (marked by the dashed white box in Figures 2b, iv, and 2c, iv). XRD patterns represent pure tetragonal phase of $CH_3NH_3PbI_3$ perovskite for samples i−iv (Figure S2, Supporting Information), showing a good agreement with previously reported perovskite on TiO_2 scaffolds.[30,38]

Good coverage of perovskite on samples i−iii renders a typical layered structure of perovskite SCs after filling the small pores inside photoanode with hole-transporting materials (HTM) (Figure 2c, i−iii). The silver electrode and photoanode were completely

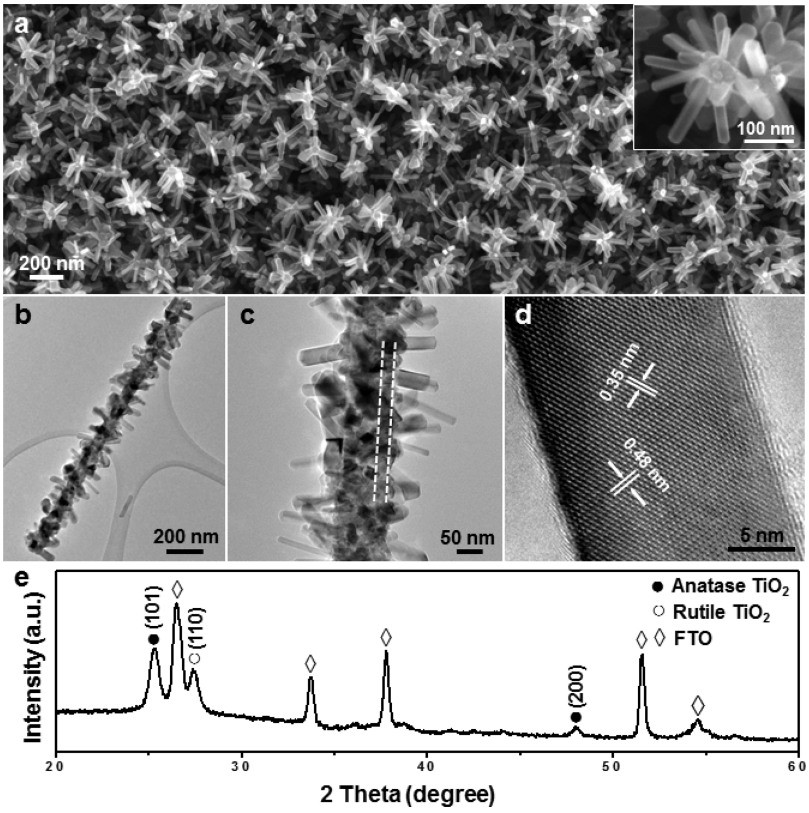

Figure 1. (a) Planar view of a 3D TiO_2 NW architecture. Inset is an enlarged SEM image showing the treelike branched NR structure. (b) TEM image of a branched TiO_2 NW showing dense and uniform coverage of TiO_2 NRs along the entire stem. (c) Higher magnification TEM image showing the single-crystalline NR branches and the polycrystalline NT trunk. (d) HRTEM image of a TiO_2 NR branch showing the perfect crystal lattice. (e) X-ray diffraction pattern of the 3D TiO_2 nanostructure revealing both anatase and rutile TiO_2 phases.

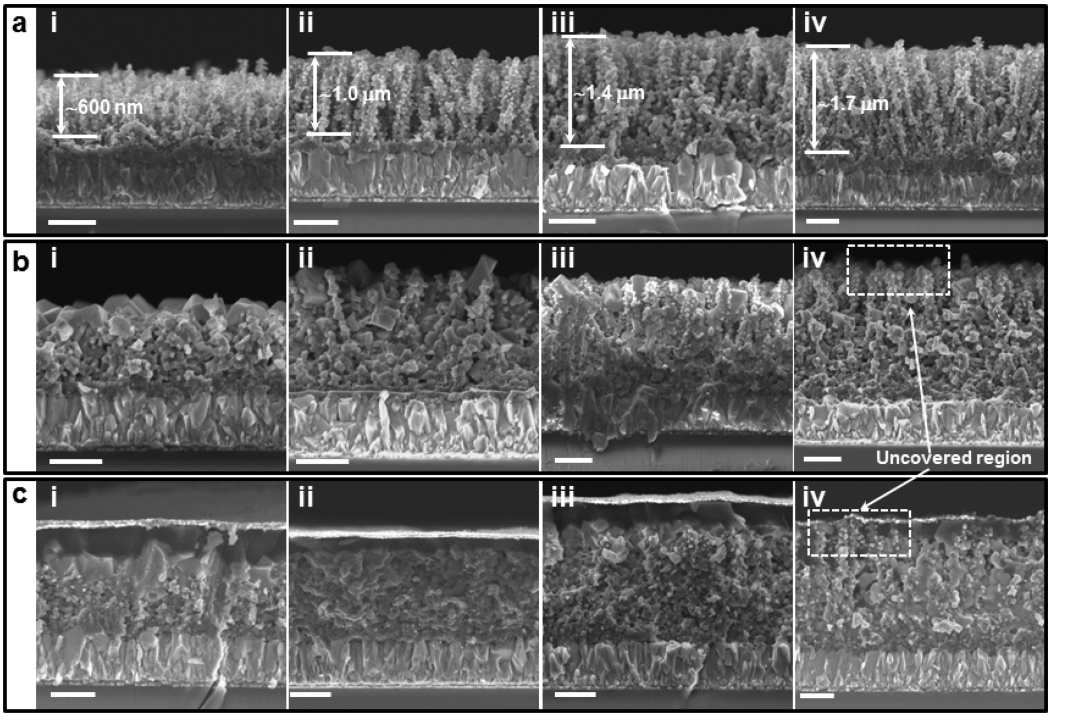

Figure 2. Cross-sectional SEM images of 3D TiO_2 nanostructures (a), $CH_3NH_3PbI_3$ perovskite coated TiO_2 (b), and the final SC devices (c). The lengths of nanostructure are ~600 nm, ~1.0 μm, ~1.4 μm, and ~1.7 μm and are marked as i, ii, iii, and iv, respectively. Scale bars are 500 nm.

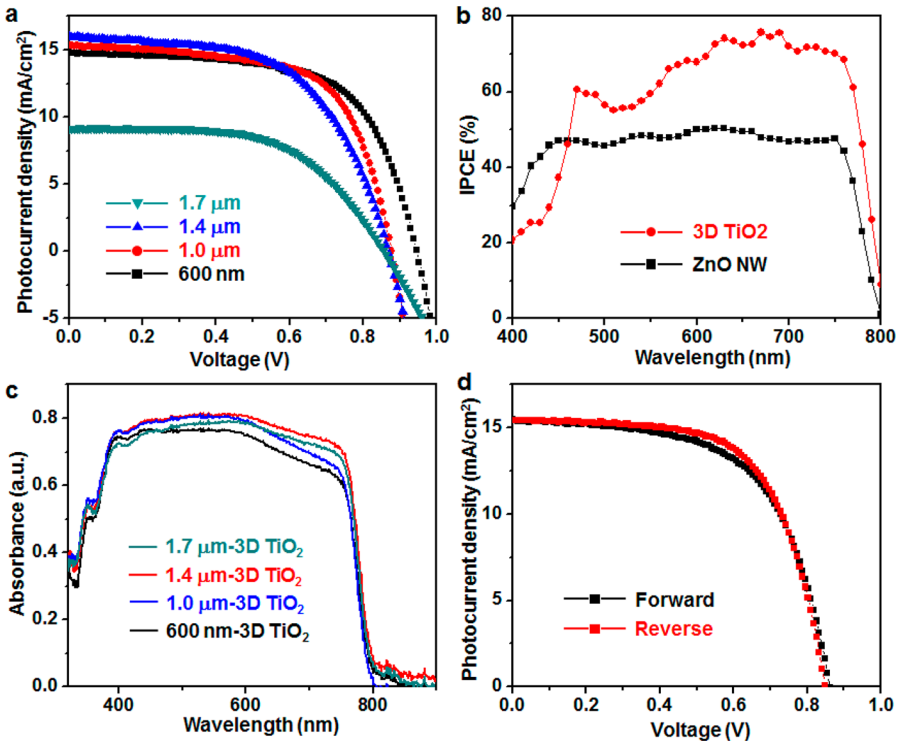

Figure 3. (a) $J-V$ curves of a series of 3D TiO_2-based perovskite SCs with different film thicknesses tested under 1 sun irradiation. (b) IPCE spectra of 3D TiO_2 (red) and ZnO NW (black) based SCs with a film thickness of ~600 nm. (c) UV–vis absorption spectra of $CH_3NH_3PbI_3$ coated 3D TiO_2 nanostructure with different film thicknesses. (d) $J-V$ curves of a cell made with ~1.4 μm 3D TiO_2/$CH_3NH_3PbI_3$/spiro-MeOTAD/Ag measured by forward (black) and reverse (red) scans with 7.5 mV voltage steps and 200 ms delay time under 1 sun illumination.

TABLE 1. PV Performances of Perovskite SCs Fabricated Using 3D TiO_2 NW Architectures with Different Lengths

	best performance				avg of 20 cells			
TiO_2 length	J_{sc} (mA/cm^2)	V_{oc} (V)	FF	η (%)	J_{sc} (mA/cm^2)	V_{oc} (V)	FF	η (%)
600 nm	14.8	0.95	0.64	9.0	13.5 ± 1.3	0.94 ± 0.1	0.63 ± 0.2	8.0 ± 1.0
1.0 μm	15.3	0.88	0.64	8.6	13.9 ± 1.4	0.87 ± 0.1	0.61 ± 0.3	7.4 ± 1.3
1.4 μm	16.0	0.87	0.58	8.1	14.4 ± 1.6	0.86 ± 0.1	0.58 ± 0.1	7.2 ± 0.9
1.7 μm	9.2	0.86	0.57	4.5	7.3 ± 1.9	0.81 ± 0.5	0.49 ± 0.8	3.1 ± 1.4

separated by the HTM layer. For sample iv, however, the open spaces are too large to be completely filled by HTM, and thus, a few NW tips touched the silver electrode (Figure S3, Supporting Information). The thickness of the HTM overlayer for samples i–iii was 289, 164, and 190 nm, respectively. The thickness of the HTM overlayer is inversely proportional to the open spaces that exist among the nanostructure scaffolds, and the largest thickness was obtained from the shortest 3D TiO_2. Similar overcoating results were also observed from mesoporous TiO_2 NP-[49] and ZnO NW-based[44] perovskite SCs.

The $J-V$ curves of perovskite SCs with different TiO_2 lengths under one sun illumination are represented in Figure 3a. In general, PCE decreased with the increase of film thickness (Table 1). This trend has also been reported from other nanostructured perovskite SCs and was suggested to be a result of declining charge generation efficiency, increased charge recombination, and raised charge-transport resistance.[20,50] The highest PCE of 9.0% was achieved from the SC made from ~600 nm long 3D TiO_2, giving a short-circuit photocurrent density (J_{sc}) of 14.8 mA/cm^2, an open-circuit voltage (V_{oc}) of 0.95 V, and a fill factor (FF) of 0.64. The average PCE of 8.0% was received by ~600 nm long 3D TiO_2 with a variation of 1.0% (Table 1). The IPCE spectrum (Figure 3b) exhibits large external quantum efficiency (EQE) of more than 70% across a wavelength range from 600 to 750 nm with a maximum of 75.7% attained at 670 nm. The onset value of 800 nm is consistent with the reported band gap of $CH_3NH_3PbI_3$ (1.55 eV).[23] Integrating the product of AM 1.5G photon flux with IPCE spectrum yields a predicted J_{sc} of 14.5 mA/cm^2, matching well with the measured J_{sc} of 14.8 mA/cm^2.

It is important to note that the IPCE at the blue and green light region is relatively lower than typical

$CH_3NH_3PbI_3$ SCs. This outcome is presumably related to the doped nature of the 3D TiO_2 nanostructure. Trace amounts of Zn residue have been observed in the TiO_2 trunk, which might enhance the electron conductivity and also narrow the band gap of TiO_2.[45] This claim is evidenced by the UV−vis absorption spectra of 3D TiO_2, where considerable absorption was recorded in the visible light region, especially at the region between 400 and 600 nm (Figure S4, Supporting Information). Such an overlap in the absorption spectra would lead to competitive light absorption between the TiO_2 framework and photoactive perovskite, resulting in lower IPCE of the SC device. In contrast, TiO_2 NTs and ZnO NWs exhibited the regular threshold of 400 nm, consistent with the band gaps of undoped TiO_2 and ZnO. To further confirm this hypothesis, the IPCE spectrum of a ZnO NW-based perovskite SC is measured. The spectrum exhibits a characteristic shape of $CH_3NH_3PbI_3$ SCs with ∼50% IPCE across almost the entire visible light region (400−750 nm). This observation suggests that the $CH_3NH_3PbI_3$ could absorb and utilize the entire visible light if no competitive absorption existed.

The PV performances of all 3D TiO_2-based SCs are summarized in Table 1. J_{sc} exhibits a relatively small dependence on the TiO_2 length and increased slightly from 14.8 mA/cm^2 for ∼600 nm to 16.0 mA/cm^2 for ∼1.4 μm. Fundamentally, J_{sc} and IPCE are determined by light-harvesting efficiency, electron and hole injection efficiency, and charge collection efficiency.[20] Electron injection efficiency is expected to be independent with length since the interfacial property between TiO_2 and $CH_3NH_3PbI_3$ should be identical regardless of length variation. Hole injection efficiency is proportional to the pore-filling fraction (PFF), which is commonly estimated by the thickness of the HTM overlayer. The thinner HTM overlayer indicates larger PFF and more effective hole injection. As shown in Figure 2c, a thinner HTM layer is observed from longer TiO_2, enabling larger PFF and hole injection efficiency and further improving J_{sc}. The light-harvesting efficiency is determined by the amount of $CH_3NH_3PbI_3$ and the optical path of incoming light. Notably, the longer TiO_2 nanostructure possesses more perovskite loading and affords higher light absorption. This is supported by the UV−vis absorption spectra (Figure 3c), where perovskite film on the longer TiO_2 framework illustrates enhanced light absorption in yellow and red light region (except the 1.7 μm sample due to its incomplete perovskite loading). To conclude, as the length of TiO_2 increases, efficiency of light harvesting and hole injection are expected to increase, while electron injection efficiency remains the same. Therefore, it is reasonable to see larger J_{sc} for longer TiO_2. However, the thicker scaffold also induces enlarged competitive absorption by TiO_2, which compensates the photocurrent enhancement and reduces the variation of J_{sc}.

TABLE 2. PV Performances of 3D TiO_2-Based Perovskite SCs under Two Scan Directions

scan direction	J_{sc} (mA/cm^2)	V_{oc} (V)	FF	η (%)
forward	15.5	0.86	0.60	8.0
reverse	15.4	0.86	0.63	8.3

V_{oc} and FF are more significantly influenced by the TiO_2 length. Starting from 0.95 V of the ∼600 nm TiO_2, V_{oc} quickly declined to 0.88 V of the ∼1 μm sample and then decreased to 0.86 V of the ∼1.4 μm one. A similar trend of V_{oc} variation has also been reported in the case of mesoporous TiO_2 NPs[50] and TiO_2 NWs.[20] It was suggested that thicker photoanode with higher surface area would increase the recombination current and therefore lead to a lower V_{oc}.[50] FF gradually deteriorated from 0.64 to 0.57 with increased nanostructure thickness, which is a consequence of the lower V_{oc} and higher electron-transport resistance.[20]

The 3D TiO_2 nanostructures were found to be effective in minimizing the hysteresis effect in perovskite SCs. The hysteresis effect has recently been recognized as a significant issue that could over- or underestimate the PCE value. Mesoporous TiO_2 NPs was reported to be superior for suppressing the hysteresis compared to planar device configurations.[28,38] Similar to the NP systems, PV performance of 3D TiO_2-based SCs demonstrated a very small hysteresis effect at a scanning delay time of 200 ms as shown in Figure 3d and Table 2. $J-V$ curves of the forward and reverse scans were almost identical. The J_{sc}, V_{oc}, and FF under reverse scan are 15.4 mA/cm^2, 0.86 V, and 0.63, respectively, yielding a PCE of 8.3%. Corresponding values for the forward scan are 15.5 mA/cm^2, 0.86 V, and 0.60, respectively, yielding a PCE of 8.0%. The largely suppressed hysteresis effect indicates the strong reliability of measured PV performance. Conversely, planar perovskite SC showed a significant hysteresis effect with a PCE of 9.5% under reverse scan and a PCE of 4.4% under the forward scan (Figure S5 and Table S1, Supporting Information). For mesoporous TiO_2 NP based perovskite SCs, low hysteresis was only achieved with the less efficient device (PCE of 5.9%), and substantial variation of PCE under forward (6.9%) and reverse (10%) was observed for well-performed cells (Figures S6 and S7 and Table S1, Supporting Information).

To demonstrate the morphological advantage of the 3D TiO_2 architecture, bare TiO_2 NTs, ZnO NWs and TiO_2-coated ZnO NWs were applied as scaffolds for fabricating perovskite SCs. Comparing the performance of these three nanostructured scaffolds clearly illustrated the morphological advantageous of the branched architecture in terms of perovskite loading, light scattering, and charge transport. Figure S8 (Supporting Information) shows the SEM images of single-crystalline ZnO NW arrays. Polycrystalline TiO_2 NTs were obtained by converting ZnO NWs following the

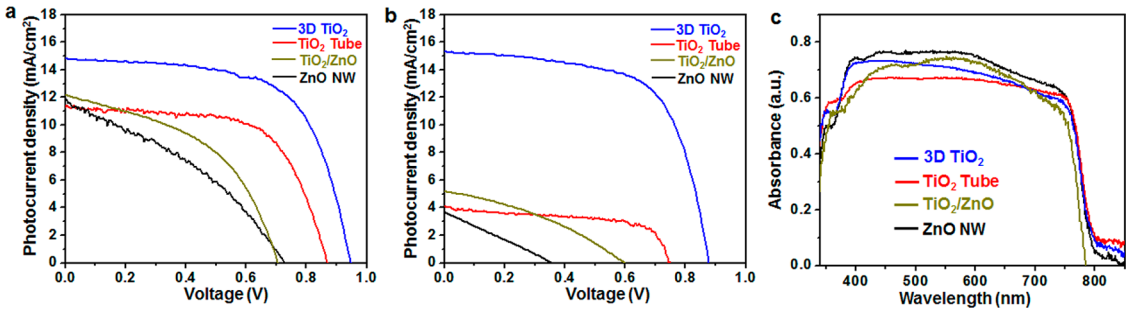

Figure 4. *J*–*V* curves of perovskite SCs made from 3D TiO_2 nanostructure, TiO_2 NTs, TiO_2-coated ZnO NWs, and ZnO NWs with an identical film thickness of ~600 nm (a) and ~1.0 μm (b). (c) UV–vis absorption spectra of $CH_3NH_3PbI_3$-coated 3D TiO_2, TiO_2 NT, TiO_2-coated ZnO NWs, and ZnO NWs with lengths of ~600 nm.

cation-exchange-driven Kirkendall effect in SPCVD reactions.[45] The SEM image (Figure S9, Supporting Information) shows the one-dimensional shape of TiO_2 NT with a rough surface. TEM characterizations in Figure S9 (Supporting Information) illustrate the hollow feature and thin polycrystalline shell. The planar and cross-sectional view of $CH_3NH_3PbI_3$ perovskite coated ZnO NWs, and the final SC devices are shown in Figure S10 (Supporting Information). Three length scales of ~600 nm, ~1.0 μm, ~1.4 μm were investigated and marked as i, ii, and iii, respectively. The TiO_2 NT-based film and device are shown in Figure S11 (Supporting Information). Figure S12 (Supporting Information) shows a TEM image of 29 nm thick TiO_2-coated ZnO NW and the corresponding perovskite film and final device configuration. As revealed by Figures S10 and S11 (Supporting Information), full coverage of $CH_3NH_3PbI_3$ perovskite and the uniform layered device structure of ZnO NWs and TiO_2 NTs were created only on the shortest nanostructures (~600 nm). A large amount of uncovered region (marked by dashed white box) can be clearly recognized when the length of nanostructure was ~1 μm and larger. This is strikingly different compared to the 3D TiO_2 structure which can effectively support perovskite as thick as ~1.4 μm. Despite the coverage, pure phased $CH_3NH_3PbI_3$ perovskite was received from both ZnO NW and TiO_2 NT scaffolds (Figure S13, Supporting Information). Although reducing the space between NWs could also facilitate a perovskite loading ratio,[44] it may need to sacrifice the total volume of perovskite and bring challenges in NW synthesis, particularly for longer NWs (e.g., >1 μm).

Morphology-related PV performances were analyzed by comparing the *J*–*V* curves of perovskite SCs fabricated from 3D TiO_2, ZnO NWs, TiO_2 NTs, and TiO_2-coated ZnO NWs with the same length of ~600 nm. 3D TiO_2 achieved a PCE of 9.0%, resulting from a J_{sc} of 14.8 mA/cm^2, a V_{oc} of 0.95 V, and a FF of 0.64. These values were all substantially higher than those of TiO_2 NT and ZnO NW. TiO_2 NTs exhibited a characteristic *J*–*V* curve shape of typical TiO_2-based perovskite SCs, offering a reasonable FF of 0.63. With a J_{sc} of 11.3 mA/cm^2 and a V_{oc} of 0.87 V, a PCE of 6.2% were obtained. Nevertheless, the ZnO NW based device only reached a J_{sc} of 11.7 mA/cm^2, a V_{oc} of 0.73 V, and a FF of 0.35, yielding a PCE of merely 3.0%. The attainable V_{oc} and FF of ZnO NW based device were apparently lower owing to the high rate of undesirable recombination compared with TiO_2 photoanodes.[51] When the film thickness increased to ~1 μm, the PCE of hierarchical TiO_2 remained as high as 8.6%. In contrast, performance of TiO_2 NT and ZnO NW declined dramatically since no typical layered configuration can be maintained, leading to tremendous loss of photocurrent, photovoltage, FF, and PCE. SCs based on TiO_2-coated ZnO NWs yielded a PCE of 4.0% with a film thickness of ~600 nm, and a similar deterioration of PCE was observed when its length increased to 1.0 μm (Table S2, Supporting Information). The heterogeneous junction between the TiO_2 film and ZnO NW may act as charge traps and lower the charge-transport efficiency.

The pronounced discrepancy of J_{sc} observed from 3D TiO_2, ZnO NWs, and TiO_2 NTs at the film thickness of ~600 nm are mainly attributed to the different light-harvesting efficiency and charge collection efficiency. As shown in Figure S1a (Supporting Information), there was an extra cap layer of $CH_3NH_3PbI_3$ cuboids on the top of 3D TiO_2, which was found to be favorable in light harvesting, charge collection, and thus boosting efficiency.[38,52] Conversely, no over layer was observed on ZnO NWs (Figure S10a–i, Supporting Information) and TiO_2 NTs (Figure S11a–i, Supporting Information), meaning lower perovskite loading and also a lack of the benefits from the bilayer structure. Moreover, branched architectures are believed to have higher light-scattering capability and, therefore, be advantageous in light harvesting.[14–16] The good light-harvesting property of 3D TiO_2 was reinforced by the absorption spectra (Figure 4c), where 3D TiO_2 clearly demonstrates larger light absorption over the entire visible light region.

The morphology-related performance variation can also be understood from the electronic transport properties and charge collection efficiency. Using conductive atomic force microscopy (C-AFM), we characterized

the conductivity of the 3D TiO_2, TiO_2 NTs, and ZnO NWs from the tips of nanostructures to the bottom electrode. $I-V$ measurements (Figure S14, Supporting Information) reveals that ZnO NW had the lowest resistivity (1.35×10^{-4} $\Omega \cdot m$ at a bias of 10 V) and polycrystalline TiO_2 NT demonstrated the highest resistivity (58.2 $\Omega \cdot m$ at a bias of 10 V).[51] The high resistance is likely a result of the polycrystalline feature of the TiO_2 NTs. The resistivity of 3D TiO_2 (3.93×10^{-2} $\Omega \cdot m$ at a bias of 10 V) was higher than that of ZnO NW but was significantly lower than that of TiO_2 NTs. The substantially improved conductivity of the 3D TiO_2 is believed to be a result of the Zn impurity residing in the TiO_2 crystals during the cation-exchange processes. Therefore, in addition to the much larger surface area, the relatively high conductivity of the 3D TiO_2 architecture is also beneficial to charge separation and transportation, which is favorable for J_{sc} and PCE improvements.

CONCLUSION

In summary, $CH_3NH_3PbI_3$ perovskite SCs were fabricated on the basis of 3D TiO_2 NW architecture. Sequentially deposited $CH_3NH_3PbI_3$ perovskite was successfully integrated onto the 3D TiO_2 framework with a length variation from ~600 nm to ~1.4 μm. In general, by increasing the length of the 3D TiO_2 scaffolds, J_{sc} was increased accordingly, while V_{oc} and FF of cells were decreased. The enlarged J_{sc} is attributed to the enhanced hole injection efficiency and increased light absorption from longer TiO_2 nanostructures. The length-related reduction of V_{oc} and FF is believed to be a result of decreased charge-generation efficiency, increased charge recombination, and higher electron-transport resistance. The best PCE was offered by the ~600 nm 3D TiO_2 scaffold with a value of 9.0%. Compared to 1D TiO_2 nanostructures made through the same process, the PCE of 3D TiO_2 was 1.5 times higher. It was even 2.3 and 2.8 times higher than that of TiO_2-coated ZnO NWs and ZnO NW-based perovskite SCs, respectively. The high-density 3D TiO_2 architecture allowed higher perovskite loading and enhanced light harvesting compared with simple 1D nanostructure arrays. C-AFM also revealed a substantially improved conductivity compared to regular TiO_2 nanostructures, which promoted the charge-transport properties. In addition, PV cells comprising 3D TiO_2 are found to be favorable in suppressing the hysteresis effect that is often observed from planar perovskite SCs. Compared to the best performed $CH_3NH_3PbI_3$ perovskite solar devices, the efficiency of the 3D TiO_2 based one is still a little lower. One possible reason is the competitive light absorption induced by the doped essence of 3D TiO_2, which could negatively affect the light harvesting by perovskite and subsequently hamper J_{sc} of the device. Nevertheless, the 3D hierarchical NWs morphology has convincingly shown advantages in terms of photoactive materials loading, electron delivering, and light scattering. It offers a promising candidate for understanding the property–performance relationship in perovskite solar cells and developing high-performance solar energy harvesting devices.

METHODS

Synthesis of ZnO NW Array Templates. FTO glasses were cleaned by ultrasonication in a series of media including an alkaline, aqueous washing solution, acetone, and ethanol and eventually treated under oxygen plasma cleaning for 10 min. The dense TiO_2 blocking layer on the cleaned FTO substrate was made by spin coating the solution of titanium isopropoxide (700 μmL), HCl (12 μL), and ethanol (10 mL) at 2000 rpm for 45 s, followed by annealing at 150 °C for 10 min and 500 °C for 30 min. Subsequently, a 50 nm thick ZnO film was coated by RF sputtering to act as seeds for ZnO NW growth. The substrate with seeds was immersed in the nutrient solution with the seeded surface facing downward. The nutrient solution comprised 25 mM zinc nitrate and 25 mM hexamethylenetetramine (HMT). ZnO NW length was controlled by the growing time, where 1 h and 10 min yielded ~600 nm NWs, 2 h for ~1.0 μm, 3 h and 20 min for ~ 1.4 μm, and 4 h for ~1.7 μm.

Synthesis of 3D TiO_2 NW Architecture. 3D TiO_2 NW architecture was synthesized in a homemade ALD system following the procedures described in our previous publication.[45] As-synthesized ZnO NW arrays were placed at the center of the ALD chamber. N_2 gas with a flow rate of 40 sccm was used to carry precursors into the chamber, generating a base pressure of ~4.1 Torr. $TiCl_4$ and H_2O vapors were used as the precursors and pulsed into the furnace separately with a pulsing time of 500 ms and separated by 60 s N_2 purging. Therefore, one deposition cycle involves 500 ms of H_2O pulse +60 s of N_2 purging +500 ms of $TiCl_4$ pulse +60 s of N_2 purging. The pressure change of $TiCl_4$ pulses was ~110 mTorr. The chamber temperature was remained at 600 °C during the entire growth process. Subsequently, the furnace was cooled down naturally under N_2 flow. The hollow TiO_2 NT was created after 10 cycles of deposition. 400 cycles of deposition yielded the 3D TiO_2 NW architecture. TiO_2-coated ZnO NWs were fabricated in the same ALD system by 400 cycles of TiO_2 deposition at 300 °C, yielding 29 nm thick polycrystalline TiO_2 film on ZnO NW surface.

Perovskite Solar Cell Fabrication. Sequential deposition approach was used to load perovskite onto 3D TiO_2.[30] Methylammonium iodide (CH_3NH_3I) was first synthesized following the literature.[53] Specifically, methylamine (24 mL, 33 wt % in ethanol, Aldrich) reacted with hydroiodic acid (10 mL, 27 wt % in water) in ethanol (100 mL) under nitrogen atmosphere at room temperature for 2 h. Then, the solution was evaporated at 80 °C until white colored powder of CH_3NH_3I crystal was precipitated. PbI_2 (99%, Aldrich) was dissolved in *N*,*N*-dimethylformamide under stirring at 70 °C to yield a concentration of 460 mg/mL. The PbI_2 solution was infiltrated into the 3D TiO_2, TiO_2 NT, ZnO NW, TiO_2-coated ZnO NW, and mesoporous TiO_2 scaffolds by spin coating at 3000 rpm for 30 s and dried at 70 °C for 30 min. After being cooled to room temperature, the PbI_2-coated samples were first prewetted in 2-propanol solution for 2 s and then immersed into solution of CH_3NH_3I in 2-propanol (10 mg/mL) for 70 s, followed by 2-propanol solution rinsing again. After drying in the air for several minutes, the films were heated at 70 °C for 30 min. HTM was then coated by spin coating at 2000 rpm for 45 s. HTM solution was prepared by dissolving 75 mg of (2,2′,7,7′-tetrakis(*N*,*N*-di-*p*-methoxyphenylamine)-9,9-spirobifluorene)(spiro-MeOTAD), 28 μL of 4-*tert*-butylpyridine, and 17 μL of solution that contains 520 mg/mL of lithium

bis(trifluoromethylsulfony)imide in acetonitrile into 1 mL of chlorobenzene. Finally, 100 nm of silver was deposited by thermal evaporation on the top of the device.

A planar cell in Figure S5 (Supporting Information) was fabricated according to ref 33. Briefly, 0.2 g of CH_3NH_3I and 0.578 g of PbI_2 was mixed in 1 mL of anhydrous *N*,*N*-dimethylformamide by shaking at room temperature for 15 min, and a clear $CH_3NH_3PbI_3$ solution was obtained with a concentration of 45%. Sequentially, 100 μL of $CH_3NH_3PbI_3$ solution was dropped onto TiO_2-coated FTO substrate and spun at 5000 rpm. After spinning at 5000 rpm for 5 s, 100 μL anhydrous chlorobenzene was quickly dropped onto the center of the substrate and then the color of substrate was changed to light brown. Total spin time was 30 s.

The mesoporous TiO_2 layer composed of 20 nm-sized particles was deposited by spin coating at 2000 rpm for 60 s using a commercial TiO_2 paste (Dyesol 18NRT, Dyesol) diluted in terpineol (1:3, weight ratio). After drying at 150 °C for 15 min, the TiO_2 films were gradually heated to 500 °C and baked at this temperature for 30 min.

Device Characterization. *J*−*V* curves were measured with a solar simulator equipped with 150 W xenon lamp (6255, Newport) and Keithley 2636 source-meter. The light intensity was adjusted to 1 sun (100 mW/cm^2), and the active area was confined to 0.785 mm^2. The IPCE was measured with a quartz tungsten halogen lamp modulated by a chopper wheel and a monochromator. The signal was recorded using a Stanford Research Systems lock-in amplifier at zero-bias and calibrated photodiodes (818 series, Newport). SEM characterizations were performed on Zeiss Leo 1530 field-emission microscope and TEM measurements were conducted on FEI TF30. X-ray diffraction pattern were acquired from the Bruker D8 Discovery with Cu Kα radiation.

UV−vis Absorption Measurement. Two machines were used to measure the absorption spectra. The absorption spectra on Figures 3c and 4c were recorded using an Evolution 220 UV−vis spectrophotometer with integrated sphere (ISA 220). Absorption was acquired by separately measuring the reflectance (%*R*) and transmittance (%*T*) spectra and using the formula $A = 1 - \%R - \%T$. A blank spectrum consisting of FTO only was measured and subtracted. The spectra of TiO_2 and ZnO on Figure S4 (Supporting Information) were obtained *via* UV−vis spectroscopy (Agilent 8453) with a direct measurement of absorption.

Conductive-Atomic Force Microscopy (C-AFM). C-AFM data were recorded using XE-70 Park Systems. Samples were glued onto a steel disk. Part of the FTO surface was exposed and connected to the AFM stage using a Au wire. The AFM was operated in contact mode with a platinum cantilever. When the AFM tip touched the top of nanostructures, the *I*−*V* curve was collected by the AFM system. Voltage was swept from 0 to 10 V.

Conflict of Interest: The authors declare no competing financial interest.

Acknowledgment. Research primarily supported by the U.S. Department of Energy (DOE), Office of Science, Basic Energy Sciences (BES), under Award No. DE-SC0008711. D.G. acknowledges the support of the National Science Foundation under Award No. CMMI-1148919 for work on AFM-based characterizations. M.A. and J.W. thank the support of Air Force Office of Scientific Research under grant # FA9550-12-1-0063 (provide facility and assistance for photovoltaic characterization).

Supporting Information Available: Additional SEM images and XRD patterns of perovskite-coated 3D TiO_2, UV−vis absorption of TiO_2 and ZnO scaffolds, I−V curves, IPCE and SEM images of planar and mesoporous TiO_2-based perovskite solar cells, SEM, XRD, and TEM characterizations of perovskite-coated ZnO NWs, TiO_2 tube and TiO_2/ZnO, *I*−*V* measurements from C-AFM for comparing the conductivity of 3D TiO_2, TiO_2 tube and ZnO NWs, and tables for photovoltaic performance of control devices. This material is available free of charge *via* the Internet at http://pubs.acs.org

REFERENCES AND NOTES

1. Gratzel, M. Photoelectrochemical Cells. *Nature* **2001**, *414*, 338–344.
2. Cheng, C.; Fan, H. J. Branched Nanowires: Synthesis and Energy Applications. *Nano Today* **2012**, *7*, 327–343.
3. Wang, X.; Li, Z.; Shi, J.; Yu, Y. One-Dimensional Titanium Dioxide Nanomaterials: Nanowires, Nanorods, and Nanobelts. *Chem. Rev.* **2014**, article ASAP.
4. Cho, I. S.; Chen, Z.; Forman, A. J.; Kim, D. R.; Rao, P. M.; Jaramillo, T. F.; Zheng, X. Branched TiO_2 Nanorods for Photoelectrochemical Hydrogen Production. *Nano Lett.* **2011**, *11*, 4978–4984.
5. Liu, C.; Tang, J.; Chen, H. M.; Liu, B.; Yang, P. A Fully Integrated Nanosystem of Semiconductor Nanowires for Direct Solar Water Splitting. *Nano Lett.* **2013**, *13*, 2989–2992.
6. Shi, J.; Hara, Y.; Sun, C.; Anderson, M. A.; Wang, X. Three-Dimensional High-Density Hierarchical Nanowire Architecture for High-Performance Photoelectrochemical Electrodes. *Nano Lett.* **2011**, *11*, 3413–3419.
7. Shi, J.; Wang, X. Hierarchical TiO_2−Si Nanowire Architecture with Photoelectrochemical Activity under Visible Light Illumination. *Energy Environ. Sci.* **2012**, *5*, 7918–7922.
8. Kargar, A.; Sun, K.; Jing, Y.; Choi, C.; Jeong, H.; Zhou, Y.; Madsen, K.; Naughton, P.; Jin, S.; Jung, G. Y.; *et al.* Tailoring n-ZnO/p-Si Branched Nanowire Heterostructures for Selective Photoelectrochemical Water Oxidation or Reduction. *Nano Lett.* **2013**, *13*, 3017–3022.
9. Kargar, A.; Sun, K.; Jing, Y.; Choi, C.; Jeong, H.; Jung, G. Y.; Jin, S.; Wang, D. 3D Branched Nanowire Photoelectrochemical Electrodes for Efficient Solar Water Splitting. *ACS Nano* **2013**, *7*, 9407–9415.
10. Sheng, W.; Sun, B.; Shi, T.; Tan, X.; Peng, Z.; Liao, G. Quantum Dot-Sensitized Hierarchical Micro/Nanowire Architecture for Photoelectrochemical Water Splitting. *ACS Nano* **2014**, *8*, 7163–7169.
11. Kargar, A.; Jing, Y.; Kim, S. J.; Riley, C. T.; Pan, X.; Wang, D. ZnO/CuO Heterojunction Branched Nanowires for Photoelectrochemical Hydrogen Generation. *ACS Nano* **2013**, *7*, 11112–11120.
12. Sauvage, F.; Di Fonzo, F.; Li Bassi, A.; Casari, C. S.; Russo, V.; Divitini, G.; Ducati, C.; Bottani, C. E.; Comte, P.; Graetzel, M. Hierarchical TiO_2 Photoanode for Dye-sensitized Solar Cells. *Nano Lett.* **2010**, *10*, 2562–2567.
13. Sheng, X.; He, D.; Yang, J.; Zhu, K.; Feng, X. Oriented Assembled TiO_2 Hierarchical Nanowire Arrays with Fast Electron Transport Properties. *Nano Lett.* **2014**, *14*, 1848–1852.
14. Wu, W. Q.; Lei, B. X.; Rao, H. S.; Xu, Y. F.; Wang, Y. F.; Su, C. Y.; Kuang, D. B. Hydrothermal Fabrication of Hierarchically Anatase TiO_2 Nanowire Arrays on FTO Glass for Dye-Sensitized Solar Cells. *Sci. Rep.* **2013**, *3*, 1352.
15. Wu, W. Q.; Feng, H. L.; Rao, H. S.; Xu, Y. F.; Kuang, D. B.; Su, C. Y. Maximizing Omnidirectional Light Harvesting in Metal Oxide Hyperbranched Array Architectures. *Nat. Commun.* **2014**, *5*, 3968.
16. Wu, W. Q.; Xu, Y. F.; Rao, H. S.; Su, C. Y.; Kuang, D. B. Multistack Integration of Three-Dimensional Hyperbranched Anatase Titania Architectures for High-eEfficiency Dye-Sensitized Solar Cells. *J. Am. Chem. Soc.* **2014**, *136*, 6437–6445.
17. Roh, D. K.; Chi, W. S.; Jeon, H.; Kim, S. J.; Kim, J. H. High Efficiency Solid-State Dye-Sensitized Solar Cells Assembled with Hierarchical Anatase Pine Tree-like TiO_2 Nanotubes. *Adv. Funct. Mater.* **2014**, *24*, 379–386.
18. Shao, F.; Sun, J.; Gao, L.; Yang, S.; Luo, J. Forest-Like TiO_2 Hierarchical Structures for Efficient Dye-Sensitized Solar Cells. *J. Mater. Chem.* **2012**, *22*, 6824–6830.
19. Wu, W.-Q.; Rao, H.-S.; Feng, H.-L.; Chen, H.-Y.; Kuang, D.-B.; Su, C.-Y. A Family of Vertically Aligned Nanowires with Smooth, Hierarchical and Hyperbranched Architectures for Efficient Energy Conversion. *Nano Energy* **2014**, *9*, 15–24.
20. Mitzi, D. B. Templating and Structural Engineering in Organic−Inorganic Perovskites. *J. Chem. Soc., Dalton Trans.* **2001**, 1–12.
21. Baikie, T.; Fang, Y.; Kadro, J. M.; Schreyer, M.; Wei, F.; Mhaisalkar, S. G.; Graetzel, M.; White, T. J. Synthesis and

Crystal Chemistry of the Hybrid Perovskite $(CH_3NH_3)PbI_3$ for Solid-State Sensitised Solar Cell Applications. *J. Mater. Chem. A* **2013**, *1*, 5628–5641.
22. Stoumpos, C. C.; Malliakas, C. D.; Kanatzidis, M. G. Semiconducting Tin and Lead Iodide Perovskites with Organic Cations: Phase Transitions, High Mobilities, and Near-Infrared Photoluminescent Properties. *Inorg. Chem.* **2013**, *52*, 9019–9038.
23. Ponseca, C. S., Jr.; Savenije, T. J.; Abdellah, M.; Zheng, K.; Yartsev, A.; Pascher, T.; Harlang, T.; Chabera, P.; Pullerits, T.; Stepanov, A.; *et al.* Organometal Halide Perovskite Solar Cell Materials Rationalized: Ultrafast Charge Generation, High and Microsecond-Long Balanced Mobilities, and Slow Recombination. *J. Am. Chem. Soc.* **2014**, *136*, 5189–5192.
24. Stranks, S. D.; Eperon, G. E.; Grancini, G.; Menelaou, C.; Alcocer, M. J.; Leijtens, T.; Herz, L. M.; Petrozza, A.; Snaith, H. J. Electron-Hole Diffusion Lengths Exceeding 1 Micrometer in an Organometal Trihalide Perovskite Absorber. *Science* **2013**, *342*, 341–344.
25. Xing, G.; Mathews, N.; Sun, S.; Lim, S. S.; Lam, Y. M.; Gratzel, M.; Mhaisalkar, S.; Sum, T. C. Long-Range Balanced Electron- and Hole-Transport Lengths in Organic-Inorganic $CH_3NH_3PbI_3$. *Science* **2013**, *342*, 344–347.
26. Gratzel, M. The Light and Shade of Perovskite Solar Cells. *Nat. Mater.* **2014**, *13*, 838–842.
27. Edri, E.; Kirmayer, S.; Henning, A.; Mukhopadhyay, S.; Gartsman, K.; Rosenwaks, Y.; Hodes, G.; Cahen, D. Why Lead Methylammonium Tri-Iodide Perovskite-Based Solar Cells Require A Mesoporous Electron Transporting Scaffold (But Not Necessarily a Hole Conductor). *Nano Lett.* **2014**, *14*, 1000–1004.
28. Burschka, J.; Pellet, N.; Moon, S. J.; Humphry-Baker, R.; Gao, P.; Nazeeruddin, M. K.; Gratzel, M. Sequential Deposition as a Route to High-Performance Perovskite-Sensitized Solar Cells. *Nature* **2013**, *499*, 316–319.
29. Liu, M.; Johnston, M. B.; Snaith, H. J. Efficient Planar Heterojunction Perovskite Solar Cells by Vapour Deposition. *Nature* **2013**, *501*, 395–398.
30. Zhou, H.; Chen, Q.; Li, G.; Luo, S.; Song, T. B.; Duan, H. S.; Hong, Z.; You, J.; Liu, Y.; Yang, Y. Interface Engineering of Highly Efficient Perovskite Solar Cells. *Science* **2014**, *345*, 542–546.
31. Liu, D.; Kelly, T. L. Perovskite Solar Cells with a Planar Heterojunction Structure Prepared Using Room-Temperature Solution Processing Techniques. *Nat. Photonics* **2013**, *8*, 133–138.
32. Chen, Q.; Zhou, H.; Hong, Z.; Luo, S.; Duan, H. S.; Wang, H. H.; Liu, Y.; Li, G.; Yang, Y. Planar Heterojunction Perovskite Solar Cells *via* Vapor-Assisted Solution Process. *J. Am. Chem. Soc.* **2014**, *136*, 622–625.
33. Xiao, M.; Huang, F.; Huang, W.; Dkhissi, Y.; Zhu, Y.; Etheridge, J.; Gray-Weale, A.; Bach, U.; Cheng, Y. B.; Spiccia, L. A Fast Deposition-Crystallization Procedure for Highly Efficient Lead Iodide Perovskite Thin-Film Solar Cells. *Angew. Chem., Int. Ed.* **2014**, *126*, 10056–10061.
34. Docampo, P.; Hanusch, F.; Stranks, S. D.; Döblinger, M.; Feckl, J. M.; Ehrensperger, M.; Minar, N. K.; Johnston, M. B.; Snaith, H. J.; Bein, T. Solution Deposition-Conversion for Planar Heterojunction Mixed Halide Perovskite Solar Cells. *Adv. Energy Mater.* **2014**, online.
35. Yella, A.; Heiniger, L. P.; Gao, P.; Nazeeruddin, M. K.; Gratzel, M. Nanocrystalline Rutile Electron Extraction Layer Enables Low-Temperature Solution Processed Perovskite Photovoltaics with 13.7% Efficiency. *Nano Lett.* **2014**, *14*, 2591–2596.
36. Jeon, N. J.; Noh, J. H.; Kim, Y. C.; Yang, W. S.; Ryu, S.; Seok, S. I. Solvent Engineering for High-Performance Inorganic-Organic Hybrid Perovskite Solar Cells. *Nat. Mater.* **2014**, *13*, 897–903.
37. Mei, A.; Li, X.; Liu, L.; Ku, Z.; Liu, T.; Rong, Y.; Xu, M.; Hu, M.; Chen, J.; Yang, Y.; et al. A Hole-Conductor-Free, Fully Printable Mesoscopic Perovskite Solar Cell with High Stability. *Science* **2014**, *345*, 295–298.
38. McGehee, M. D. Perovskite Solar Cells: Continuing to Soar. *Nat. Mater.* **2014**, *13*, 845–846.
39. Editorial. Perovskite Fever. *Nat. Mater.* **2014**, *13*, 837.
40. Unger, E. L.; Hoke, E. T.; Bailie, C. D.; Nguyen, W. H.; Bowring, A. R.; Heumuller, T.; Christoforo, M. G.; McGehee, M. D. Hysteresis and Transient Behavior in Current-Voltage Measurements of Hybrid-Perovskite Absorber Solar Cells. *Energy Environ. Sci.* **2014**, advance article.
41. Kim, H. S.; Lee, J. W.; Yantara, N.; Boix, P. P.; Kulkarni, S. A.; Mhaisalkar, S.; Gratzel, M.; Park, N. G. High Efficiency Solid-State Sensitized Solar Cell-Based on Submicrometer Rutile TiO_2 Nanorod and $CH_3NH_3PbI_3$ Perovskite Sensitizer. *Nano Lett.* **2013**, *13*, 2412–2417.
42. Dharani, S.; Mulmudi, H. K.; Yantara, N.; Thu Trang, P. T.; Park, N. G.; Graetzel, M.; Mhaisalkar, S.; Mathews, N.; Boix, P. P. High Efficiency Electrospun TiO_2 Nanofiber Based Hybrid Organic-Inorganic Perovskite Solar Cell. *Nanoscale* **2014**, *6*, 1675–1679.
43. Kumar, M. H.; Yantara, N.; Dharani, S.; Graetzel, M.; Mhaisalkar, S.; Boix, P. P.; Mathews, N. Flexible, Low-Temperature, Solution Processed ZnO-Based Perovskite Solid State Solar Cells. *Chem. Commun.* **2013**, *49*, 11089–11091.
44. Son, D.-Y.; Im, J.-H.; Kim, H.-S.; Park, N.-G. 11% Efficient Perovskite Solar Cell Based on ZnO Nanorods: An Effective Charge Collection System. *J. Phys. Chem. C* **2014**, *118*, 16567–16573.
45. Yu, Y.; Yin, X.; Kvit, A.; Wang, X. Evolution of Hollow TiO_2 Nanostructures *via* the Kirkendall Effect Driven by Cation Exchange with Enhanced Photoelectrochemical Performance. *Nano Lett.* **2014**, *14*, 2528–2535.
46. Shi, J.; Sun, C.; Starr, M. B.; Wang, X. Growth of Titanium Dioxide Nanorods in 3D-Confined Spaces. *Nano Lett.* **2011**, *11*, 624–631.
47. Shi, J.; Li, Z.; Kvit, A.; Krylyuk, S.; Davydov, A. V.; Wang, X. Electron Microscopy Observation of TiO_2 Nanocrystal Evolution in High-Temperature Atomic Layer Deposition. *Nano Lett.* **2013**, *13*, 5727–5734.
48. Law, M.; Greene, L. E.; Johnson, J. C.; Saykally, R.; Yang, P. Nanowire Dye-Sensitized Solar Cells. *Nat. Mater.* **2005**, *4*, 455–459.
49. Ding, I. K.; Tétreault, N.; Brillet, J.; Hardin, B. E.; Smith, E. H.; Rosenthal, S. J.; Sauvage, F.; Grätzel, M.; McGehee, M. D. Pore-Filling of Spiro-OMeTAD in Solid-State Dye Sensitized Solar Cells: Quantification, Mechanism, and Consequences for Device Performance. *Adv. Funct. Mater.* **2009**, *19*, 2431–2436.
50. Kim, H. S.; Lee, C. R.; Im, J. H.; Lee, K. B.; Moehl, T.; Marchioro, A.; Moon, S. J.; Humphry-Baker, R.; Yum, J. H.; Moser, J. E.; *et al.* Lead Iodide Perovskite Sensitized All-Solid-State Submicron Thin Film Mesoscopic Solar Cell with Efficiency Exceeding 9%. *Sci. Rep.* **2012**, *2*, 591.
51. Chandiran, A. K.; Abdi-Jalebi, M.; Nazeeruddin, M. K.; Gratzel, M. Analysis of Electron Transfer Properties of ZnO and TiO_2 Photoanodes for Dye-Sensitized Solar Cells. *ACS Nano* **2014**, *8*, 2261–2268.
52. Im, J. H.; Jang, I. H.; Pellet, N.; Gratzel, M.; Park, N. G. Growth of $CH_3NH_3PbI_3$ Cuboids with Controlled Size for High-Efficiency Perovskite Solar Cells. *Nat. Nanotechnol.* **2014**, online.
53. Lee, M. M.; Teuscher, J.; Miyasaka, T.; Murakami, T. N.; Snaith, H. J. Efficient Hybrid Solar Cells Based on Meso-Superstructured Organometal Halide Perovskites. *Science* **2012**, *338*, 643–647.